

Dynamic physiological modeling for functional diffuse optical tomography

Solomon Gilbert Diamond,^{a,*} Theodore J. Huppert,^a Ville Kolehmainen,^b
Maria Angela Franceschini,^a Jari P. Kaipio,^b Simon R. Arridge,^c and David A. Boas^a

^aMassachusetts General Hospital, Athinoula A. Martinos Center for Biomedical Imaging, Charlestown, MA 02129, USA

^bDepartment of Applied Physics, University of Kuopio, PO Box 1627, 70211 Kuopio, Finland

^cDepartment of Computer Science, University College London, Gower Street, London WC1E 6BT, UK

Received 1 August 2005; accepted 14 September 2005

Available online 20 October 2005

Diffuse optical tomography (DOT) is a noninvasive imaging technology that is sensitive to local concentration changes in oxy- and deoxy-hemoglobin. When applied to functional neuroimaging, DOT measures hemodynamics in the scalp and brain that reflect competing metabolic demands and cardiovascular dynamics. The diffuse nature of near-infrared photon migration in tissue and the multitude of physiological systems that affect hemodynamics motivate the use of anatomical and physiological models to improve estimates of the functional hemodynamic response. In this paper, we present a linear state-space model for DOT analysis that models the physiological fluctuations present in the data with either static or dynamic estimation. We demonstrate the approach by using auxiliary measurements of blood pressure variability and heart rate variability as inputs to model the background physiology in DOT data. We evaluate the improvements accorded by modeling this physiology on ten human subjects with simulated functional hemodynamic responses added to the baseline physiology. Adding physiological modeling with a static estimator significantly improved estimates of the simulated functional response, and further significant improvements were achieved with a dynamic Kalman filter estimator (paired *t* tests, $n = 10$, $P < 0.05$). These results suggest that physiological modeling can improve DOT analysis. The further improvement with the Kalman filter encourages continued research into dynamic linear modeling of the physiology present in DOT. Cardiovascular dynamics also affect the blood-oxygen-dependent (BOLD) signal in functional magnetic resonance imaging (fMRI). This state-space approach to DOT analysis could be extended to BOLD fMRI analysis, multimodal studies and real-time analysis.

© 2005 Elsevier Inc. All rights reserved.

Keywords: Physiological modeling; State-space model; Near-infrared spectroscopy; Diffuse optical tomography; Kalman filter; Time-series analysis

Introduction

Diffuse optical tomography (DOT) is a noninvasive imaging technology that uses near-infrared (IR) light to image biological tissue. The dominant chromophores in this spectrum are oxy-hemoglobin (HbO), deoxyhemoglobin (HbR), lipids and water. The basis of DOT is in vivo dynamic near-infrared spectroscopy of these dominant chromophores in the tissue. Tomographic images in DOT are constructed by simultaneously measuring from many regions that cover a larger volume of tissue. The achievable in-plane resolution of DOT decreases rapidly with depth because biological tissue is a highly scattering medium for near-infrared light. This diffuse property of the light also limits the penetration depth in the adult human brain imaging to about 3 cm, which is sufficient to study most of the cerebral cortex. See Gibson et al. (2005a) for a more complete description of DOT. Clinical and research applications of DOT arise due to its specificity to the physiologically relevant chromophores HbO and HbR. Potential clinical and research applications for DOT abound in brain injury (Vernieri et al., 1999; Chen et al., 2000; Nemoto et al., 2000; Saitou et al., 2000), neurological diseases (Hock et al., 1996; Fallgatter et al., 1997; Hanlon et al., 1999; Steinhoff et al., 1996; Adelson et al., 1999; Sokol et al., 2000; Watanabe et al., 2000), psychiatric disorders (Okada et al., 1996b; Eschweiler et al., 2000; Matsuo et al., 2000; Okada et al., 1994; Fallgatter and Strik, 2000) and in cognitive and behavioral neuroscience (Ruben et al., 1997; Sakatani et al., 1999; Franceschini et al., 2003; Colier et al., 1999; Sato et al., 1999). Other research areas for DOT include infant monitoring (Chen et al., 2002; Hintz et al., 2001; Meek et al., 1999; Baird et al., 2002; Pena et al., 2003; Taga et al., 2003) and breast cancer detection (Jakubowski et al., 2004; Shah et al., 2004; Dehghani et al., 2003; Srinivasan et al., 2003). DOT is particularly suitable for in situ monitoring and multimodal imaging (Strangman et al., 2002). The dynamics measured with DOT in the functional neuroimaging application are caused by dynamics in blood volume and oxygenation in the scalp and in the brain. The measured

* Corresponding author.

E-mail address: sdiamond@nmr.mgh.harvard.edu (S.G. Diamond).

Available online on ScienceDirect (www.sciencedirect.com).

hemodynamics are caused by systemic fluctuations associated with cardiac pulsation, respiration, heart rate variations, vasomotion and the vascular response to neuronal activity (Obrig et al., 2000; Toronov et al., 2000).

The primary aim of DOT functional neuroimaging is to localize and separate the stimulus-related brain function signal from the background physiology. The main problems are that the background physiology is much stronger than the stimulus response and that anatomical regions are mixed in the diffuse measurements. As a result, the DOT inverse problem cannot be solved without some prior knowledge about the relevant anatomy and physiology. Since the nature of functional anatomy is that structure and function are mutually informative, spatial and temporal prior knowledge should be considered in concert. The challenge of DOT analysis is then to design a framework that will accommodate spatiotemporal prior knowledge in a numerically tractable inverse problem. We attempt here to advance DOT analysis in this direction.

Biophysical modeling of near-infrared photon migration in human tissue remains an active area of research. Although a forward model of the relevant physics is captured by the radiative transport equation (Chandrasekhar, 1960), its solution for the complex geometry of the human head can only be approximated. One approach is to apply a finite element numerical solution to the diffusion approximation to the transport equation (Arridge, 1999). Another approach is to use hybrid methods (Ripoll et al., 2001; Hayashi et al., 2003). Others have used a Monte Carlo simulation of the photon migration (Okada et al., 1996a; Fukui et al., 2003; Boas et al., 2002). Optical absorption and scattering parameters for different tissue types are still debated in the literature (Koyama et al., 2005; Strangman et al., 2003). The spatial inverse problem is highly ill posed and requires regularization. Both linear (Boas et al., 2004b; Yamamoto et al., 2002; Hintz et al., 2001) and nonlinear (Bluestone et al., 2001; Prince et al., 2003; Xu et al., 2005; Hebden et al., 2004) reconstructions are commonly used in DOT.

Many physiological systems are involved in determining the vascular, blood pressure and blood oxygen dynamics in the scalp and brain during DOT functional neuroimaging experiments. Models of the systemic cardiovascular system (Mukkamala and Cohen, 2001) and cerebral autoregulation (Lu et al., 2004) demonstrate how these complex systems interact to produce the observed short-term physiological variability. Some of the key factors are heart rate, stroke volume, arterial and venous compliance. These cardiovascular parameters are mediated by autonomic regulatory mechanisms such as the arterial and cardiopulmonary baroreflexes and by cardiorespiratory coupling in the medulla. Cerebral autoregulation maintains relatively constant cerebral blood flow (CBF) irrespective of variations in arterial blood pressure. Despite this autoregulation, short-term variability in CBF is still present (Panerai, 2004). Local vasomotion is also present throughout the brain and introduces spatial and temporal variability in hemodynamics (Mayhew et al., 1996). Local cerebral vascular beds respond to the metabolic demands of neurons with a localized increase in blood flow, which is called the neurovascular response (Logothetis et al., 2001). Systemic blood oxygen and cerebral hemodynamics are also affected by inspired gas concentrations and ventilation rate (Rostrup et al., 2002).

One method to help separate out the background physiology in neuroimaging data is to include noninvasive auxiliary physiological measurements as inputs in the analysis. Many instruments can be used during experiments to acquire these physiological dynamics. Examples are the blood pressure monitor, pulse

oximeter, electrocardiogram (ECG), chest band respirometer, spirometer and capnograph. Stationary linear regression methods in fMRI analysis (Frackowiak et al., 2003) accept multiple regressors that could easily include auxiliary physiological measurements. Including these additional inputs is a small extension of standard finite impulse response (FIR) deconvolution techniques (Goutte et al., 2000), which make the assumption that the FIR models are time invariant. Zwiener et al. (2001) investigated short-term coordinations between respiratory movements, heart rate fluctuations and arterial blood pressure fluctuations with partial coherence analysis. They concluded that there are direct and changing coordinations between all three parameters to different extents within the respiratory frequency range even during paced breathing. These changing coordinations suggest that the physiological effects are non-stationary and that dynamic analysis methods may be more appropriate.

Dynamical methods in fMRI analysis have been applied with parametric models of the functional response and a wide variety of statistical methods (Gössl et al., 2000; Riera et al., 2004; Friston, 2002). These methods from fMRI are not directly transferable to DOT because of differences in the biophysical models and relative spatial and temporal resolution. In the DOT literature, Kolehmainen et al. (2003) applied dynamic state-space estimation without physiological regressors. Prince et al. (2003) fit the amplitude and phase angle of three non-stationary sinusoids to DOT time-series data using the Kalman filter. The three sinusoids were intended to model the cardiac pulsations, respiratory affects and functional response to a blocked experimental design. While supporting the principle of using the dynamic Kalman filter in DOT analysis, the three-sinusoid model does not allow for the most commonly used event-related experimental designs nor can it use readily available physiological measurements such as blood pressure as a regressor. Zhang et al. (2005b) used principal component analysis (PCA) to reduce the background physiological variance in functional neuroimaging experiments. Anecdotal evidence was presented that certain principal components correlate with blood pressure and respiratory dynamics, but, since PCA analysis does not accept exogenous inputs, any additional information contained in the physiological measurements is not actually used. Known respiratory interactions in blood pressure regulation (Cohen and Taylor, 2002) suggest that the orthogonal projections in PCA are likely to be mixtures of physiological effects. Due to the blind nature of PCA, it is unclear how the principal components relate to prior information from anatomical and physiological models.

In this paper, we present a state-space model that incorporates most of the relevant anatomy, physiology and physics for DOT. Unknown parameters in the proposed model can then be estimated with the static and dynamic methods that we discuss. We evaluate the model on data from ten human subjects with simulated local hemodynamic responses added to the baseline physiology. With this evaluation method, we confirm that the simulated activations can be recovered and compare the results with and without physiological inputs and from static and dynamic estimators.

A state-space model for DOT

We illustrate the anatomy, physiology and physics related to DOT in the schematic of Fig. 1a with a level of complexity that is intended to facilitate the design of a state-space analog. Within the model, an experimental design determines the timing of events to

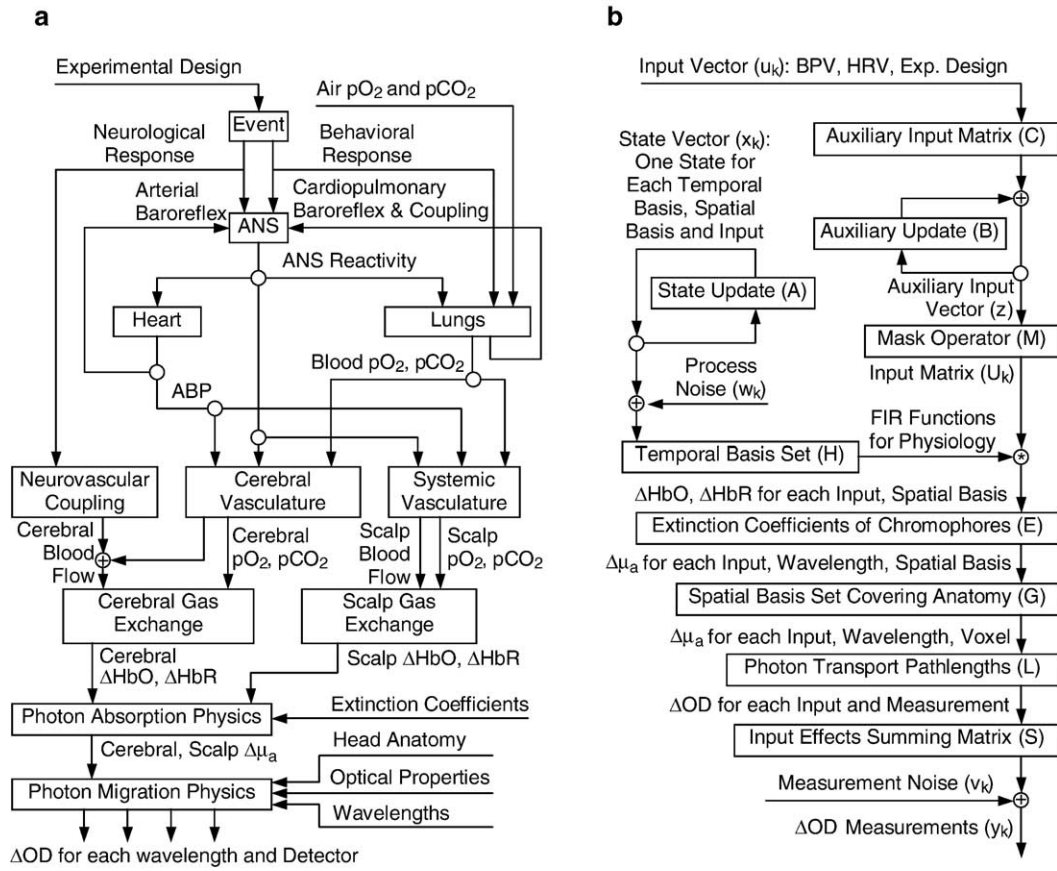


Fig. 1. The proposed state-space model shown on the right is designed to capture the main elements of the relevant anatomy, physiology and physics shown on the left in a linear formulation. The specifics of the state-space model are defined in the text along with all acronyms and variables' names. (a) Anatomy, physiology and physics for DOT. (b) State-Space Model for DOT analysis.

which the subject responds neurologically and behaviorally. The neurological response leads to changes in local cerebral blood flow through a neurovascular coupling mechanism. Blood flow changes are also caused by cerebrovascular autoregulation, through which effects can propagate from the systemic physiology. Cerebral blood oxygen saturation and blood flow undergo gas exchange with the brain tissue resulting in the cerebral hemodynamics. The model also contains hemodynamic contributions from the scalp, which are determined from the blood flow and oxygenation from the systemic vasculature. The systemic inputs are the arterial blood pressure (ABP) from the heart, the partial pressures of oxygen (pO_2) and carbon dioxide (pCO_2) from the lungs and autonomic nervous system (ANS) reactivity, which affects vasomotion. The cerebral and scalp hemodynamics cause dynamics in the absorption property of the tissues. These dynamics are superimposed on the background tissue optical properties. Photon migration physics determine the DOT measurements from the head anatomy and the optical properties of the skin, muscle, fat, blood vessels, bone, bone marrow, cerebrospinal fluid (CSF), dura, gray and white matter.

A schematic for the state-space model we propose for linear system identification is illustrated in Fig. 1b. ABP, ANS reactivity and blood gas concentrations are approximately quantified with noninvasive correlates. ABP approximately correlates with pressure variations measured with a finger cuff, which will be called blood pressure variability (BPV). ANS reactivity can be assessed with heart rate variability (HRV); and blood gas concentrations can be controlled by varying the gas concentrations of inspired air and

monitoring end tidal CO_2 . By combining these auxiliary data with the experimental design and DOT measurements, pathways within the physiological model in Fig. 1a can be approximated as lumped linear models. The inputs u in the state-space model are the Boolean stimulus time vector and time-series physiological measurements of BPV and HRV. Inspired gas concentrations are constant in most experiments, and so end tidal CO_2 is not often included as an input. We define the model states x to be the weights for temporal basis sets that comprise discrete FIR functions, which relate the measurable inputs to the unknown chromophore concentration changes in different regions of the tissue. In order to perform the convolution, it is convenient to define auxiliary states z that merely store a regression length n_r of most recent inputs. The measurements y are the time-series of changes in optical density (ΔOD) measured from the detectors at each wavelength. A linear biophysical model propagates the local concentration changes to the DOT measurements collected with the instrumentation. We

Table 1

Length constant names used in the specification of all state-space variables

n_u	Inputs (regressors)	n_w	Wavelengths
n_d	Source-detector pairs	n_c	Chromophores
n_s	Voxels	n_g	Spatial basis functions
n_r	Regression time points	n_h	Temporal basis functions
n_x	States ($n_x = n_u n_c n_g n_h$)	n_y	Measurements ($n_y = n_w n_d$)
n_z	Auxiliary states ($n_z = n_u n_c n_g n_r$)	n_k	Total time points

Table 2
State-space variable names

k	Time index	$\mathbf{u}_{(n_u,1)}(k)$	Input vector
$\mathbf{x}_{(n_x,1)}(k)$	State vector	$\mathbf{V}_{(n_x,n_x)}(k)$	State covariance
$\mathbf{w}_{(n_w,1)}(k)$	Process noise	$\mathbf{Q}_{(n_w,n_w)}$	Process noise covariance
$\mathbf{z}_{(n_z,1)}(k)$	Auxiliary state vector	$\mathbf{y}_{(n_y,1)}(k)$	Measurement vector
$\mathbf{v}_{(n_v,1)}(k)$	Measurement noise	$\mathbf{R}_{(n_y,n_y)}$	Measurement noise covariance
$\mathbf{A}_{(n_x,n_x)}$	State update model	$\mathbf{B}_{(n_x,n_x)}$	Auxiliary update model
$\mathbf{C}_{(n_x,n_u)}$	Auxiliary input model	$\mathbf{D}_{(n_x,n_x)}(k)$	Measurement model
$\mathbf{K}_{(n_x,n_y)}(k)$	Kalman gain matrix	$\mathbf{S}_{(n_y,n_y,n_y)}$	Summing matrix
$\mathbf{U}_{(n_u,n_u,n_g,n_z)}(k)$	Input matrix	$\mathbf{M}_{(n_u,n_u,n_g,n_z)}$	Input mask matrix
$\mathbf{L}_{(n_u,n_y,n_u,n_x)}$	Pathlength matrix	$\mathbf{L}_{0(n_y,n_u,n_x)}$	Pathlength submatrix
$\mathbf{G}_{(n_u,n_u,n_x,n_u,n_g)}$	Spatial basis set	$\mathbf{G}_{0(n_x,n_g)}$	Spatial submatrix
$\mathbf{E}_{(n_u,n_u,n_g,n_u,n_g)}$	Extinction matrix	$\mathbf{E}_{0(n_u,n_x)}$	Extinction submatrix
$\mathbf{H}_{(n_x,n_x)}$	Temporal basis set	$\mathbf{H}_{0(n_x,n_h)}$	Temporal submatrix

The respective sizes of each variable are indicated with parenthetical subscript notation and those that vary with the time index are indicated.

define all the constants and variables for the state-space model in Tables 1 and 2 and further explain the model elements subsequently.

Our state-space model shown in Fig. 1b is a discrete-time process that we will now describe in detail. In the following description, \otimes will use the notations T for the transpose operator, \otimes for the Kronecker tensor product, \odot for term-by-term array multiplication, \mathbf{I} for the identity matrix, $\mathbf{1}$ for a matrix of ones, $\mathbf{0}$ for a matrix of zeros, and matrix sizes will be indicated with parenthetical subscripts.

Starting with the input vector \mathbf{u} , the auxiliary state update described by Eq. (1) buffers the input vector \mathbf{u} into an auxiliary state vector \mathbf{z} storing n_r time points of each input. The auxiliary input model \mathbf{C} places the current time step of the input vector \mathbf{u} into its proper location in the auxiliary state vector \mathbf{z} . The auxiliary update model \mathbf{B} has a structure that advances the buffered inputs in \mathbf{z} by one time step

$$\mathbf{z}_k = \mathbf{B}\mathbf{z}_{k-1} + \mathbf{C}\mathbf{u}_k, \quad (1)$$

$$\mathbf{C} = \mathbf{I}_{(n_u)} \otimes \mathbf{1}_{(n_x n_g, 1)} \otimes \begin{bmatrix} \mathbf{1}_{(1,1)} \\ \mathbf{0}_{(n_r-1,1)} \end{bmatrix}, \quad (2)$$

$$\mathbf{B} = \mathbf{I}_{(n_u n_x n_g)} \otimes \begin{bmatrix} \mathbf{0}_{(1, n_r-1)} & \mathbf{0}_{(1,1)} \\ \mathbf{I}_{(n_r-1)} & \mathbf{0}_{(n_r-1,1)} \end{bmatrix}. \quad (3)$$

The mask matrix \mathbf{M} is used to arrange the auxiliary states into an input matrix \mathbf{U} that allows multiple convolutions with the inputs to be performed with a single matrix multiplication

$$\mathbf{M} = \mathbf{I}_{(n_u n_x n_g)} \otimes \mathbf{1}_{(1, n_r)}, \quad (4)$$

$$\mathbf{U}_k = \mathbf{1}_{(n_u n_x n_g, 1)} \mathbf{z}_k^T \odot \mathbf{M}. \quad (5)$$

The state vector \mathbf{x} in Fig. 1b contains the weights for the temporal basis set \mathbf{H} that comprises the finite impulse response functions used to model the physiology related to each input. The state update defined by Eq. (6) is a first order autoregressive model for the temporal evolution of the state vector \mathbf{x} . We have defined the state update model \mathbf{A} as an identity, which specifies no inherent growth or decay of the states. The process noise \mathbf{w} is added at each time step

$$\mathbf{x}_k = \mathbf{A}\mathbf{x}_{k-1} + \mathbf{w}_k \quad (6)$$

$$\mathbf{A} = \mathbf{I}_{(n_x)}. \quad (7)$$

The measurement update of Eq. (8) effectively filters the inputs \mathbf{u} with order $n_r - 1$ finite impulse response filters defined by the

states \mathbf{x} to predict the dynamics in the measurements \mathbf{y} . The measurement noise \mathbf{v} adds to the measurement vector \mathbf{y} at each time step. The elements of the measurement model \mathbf{D} are contained in Eq. (9) and are also shown in Fig. 1b

$$\mathbf{y}_k = \mathbf{D}(\mathbf{U}_k)\mathbf{x}_k + \mathbf{v}_k, \quad (8)$$

$$\mathbf{D}(\mathbf{U}_k) = \mathbf{S}\mathbf{L}\mathbf{G}\mathbf{E}\mathbf{U}_k\mathbf{H}. \quad (9)$$

The states \mathbf{x} operate through temporal \mathbf{H} and spatial \mathbf{G} basis sets, which have the Kronecker product structure

$$\mathbf{H} = \mathbf{I}_{(n_u n_x n_g)} \otimes \mathbf{H}_0, \quad (10)$$

$$\mathbf{G} = \mathbf{I}_{(n_u n_x)} \otimes \mathbf{G}_0. \quad (11)$$

The columns of the temporal submatrix \mathbf{H}_0 contain temporal basis functions to reduce the number of states and/or impose temporal smoothing. The columns of the spatial submatrix \mathbf{G}_0 contain a set of spatial basis functions that can be used to reduce the number of states and/or impose spatial smoothing of the state estimates.

The optical extinction coefficients for the chromophores present in the tissue volume are contained in the wavelength by chromophore submatrix \mathbf{E}_0 and then copied and arranged into the extinction matrix \mathbf{E} . The pathlength submatrix \mathbf{L}_0 is a block diagonal matrix formed from detector by voxel average effective pathlengths for each wavelength as described by Arridge et al. (1992). The pathlength matrix \mathbf{L} captures the relevant physics for linear tomographic reconstructions for the set of continuous wave measurements in \mathbf{y}

$$\mathbf{E} = \mathbf{I}_{(n_u)} \otimes \mathbf{E}_0 \otimes \mathbf{I}_{(n_g)}, \quad (12)$$

$$\mathbf{L} = \mathbf{I}_{(n_u)} \otimes \mathbf{L}_0. \quad (13)$$

The last element of the state-space model is a summing matrix \mathbf{S} , which combines the effects of multiple inputs in \mathbf{u} into the measurements \mathbf{y}

$$\mathbf{S}_k = \mathbf{1}_{(1, n_u)} \otimes \mathbf{I}_{(n_y)}. \quad (14)$$

Static least-squares estimator

For the static least-squares estimator, we first pre-calculate \mathbf{U}_k and $\mathbf{D}(\mathbf{U}_k)$ for all time steps k and then arrange the forward model

$$\mathbf{y}_s = \mathbf{D}_s \mathbf{x}, \quad (15)$$

where \mathbf{y}_s is the concatenation of \mathbf{y}_k at every time step

$$\mathbf{y}_s = \left[\mathbf{y}[1]^T \mathbf{y}[2]^T \dots \mathbf{y}[n_k]^T \right]^T, \quad (16)$$

and \mathbf{D}_s is a similar concatenation of \mathbf{D}_k

$$\mathbf{D}_s = \left[\mathbf{D}[1]^T \mathbf{D}[2]^T \dots \mathbf{D}[n_k]^T \right]^T. \quad (17)$$

We then use a standard Tikhonov or ridge regression estimator for \mathbf{x}

$$\hat{\mathbf{x}} (\mathbf{D}_s^T \mathbf{D}_s + \alpha^2 \mathbf{I}_{(nx)})^{-1} \mathbf{D}_s^T \mathbf{y}_s, \quad (18)$$

where α is the regularization parameter. There are many other linear estimators that could be used in place of Eq. (18). Kay (1993) discusses most of the common alternatives. We chose to use Tikhonov here because of its simplicity and wide general use.

Dynamic Kalman filter estimator

The Kalman filter is a recursive solution to discrete linear filtering and prediction problems such as our proposed state-space model (Kalman, 1960). The objective of the Kalman filter is to obtain the best state estimates $\hat{\mathbf{x}}_{k|k-1}$ in a mean square sense given all the data up to that time $\{\mathbf{y}_1, \dots, \mathbf{y}_k\}$. There are many ways to model the same physical system within the generality of the Kalman filter, and so the following discussion is limited to our proposed model. The Kalman filter recursions require initialization of the state vector estimate $\hat{\mathbf{x}}_0$ and estimated state covariance $\hat{\mathbf{V}}_0$. Statistical covariance priors must also be specified for the state process noise $\text{cov}(\mathbf{w}) = \mathbf{Q}$ and the measurement noise $\text{cov}(\mathbf{v}) = \mathbf{R}$. The algorithm can then proceed with the following prediction-correction recursion.

First, the auxiliary state vector \mathbf{z} and measurement model \mathbf{D} are updated

$$\mathbf{z}_{k|k-1} = \mathbf{B}\mathbf{z}_{k-1|k-1} + \mathbf{C}\mathbf{u}_k, \quad (19)$$

$$\mathbf{U}_k = \mathbf{1}_{(n_s n_e n_g, 1)} \mathbf{z}_{k|k-1}^T \odot \mathbf{M}, \quad (20)$$

$$\mathbf{D}_k = \mathbf{SLGEU}_k \mathbf{H}. \quad (21)$$

Next the state vector \mathbf{x} and state covariance \mathbf{V} are predicted

$$\hat{\mathbf{x}}_{k|k-1} = \mathbf{A}\hat{\mathbf{x}}_{k-1|k-1}, \quad (22)$$

$$\hat{\mathbf{V}}_{k|k-1} = \mathbf{A}\hat{\mathbf{V}}_{k-1|k-1}\mathbf{A}^T + \mathbf{Q}. \quad (23)$$

The Kalman gain matrix \mathbf{K} is then computed

$$\mathbf{K}_k = \hat{\mathbf{V}}_{k|k-1} \mathbf{D}_k^T (\mathbf{D}_k \hat{\mathbf{V}}_{k|k-1} \mathbf{D}_k^T + \mathbf{R})^{-1}, \quad (24)$$

and the auxiliary state vector \mathbf{z} , state vector \mathbf{x} and state covariance \mathbf{V} predictions are corrected with the new measurements \mathbf{y} that are available at time step k

$$\mathbf{z}_{k|k} = \mathbf{z}_{k|k-1}, \quad (25)$$

$$\hat{\mathbf{x}}_{k|k} = \hat{\mathbf{x}}_{k|k-1} + \mathbf{K}_k (\mathbf{y}_k - \mathbf{D}_k \hat{\mathbf{x}}_{k|k-1}), \quad (26)$$

$$\hat{\mathbf{V}}_{k|k} = \hat{\mathbf{V}}_{k|k-1} - \mathbf{K}_k \mathbf{D}_k \hat{\mathbf{V}}_{k|k-1}. \quad (27)$$

Model validation

The salient feature of the state-space model we propose for DOT analysis is physiological modeling. We designed the following experiment to validate that the model reduces physiological interference in estimates of a functional hemodynamic response. The approach we took was to add a simulated functional response to real data and then attempt to recover the simulated response. Adding a simulated response allowed us to quantitatively evaluate the analysis methods by comparing the estimated responses with the “true” response that could not be directly measured otherwise. We hypothesized that including blood pressure variability and heart rate variability as inputs \mathbf{u} would model some of the real physiological variance and thereby improve estimates of the simulated response. We also hypothesized that allowing dynamic estimation of the physiological models would further improve the simulated response estimates.

Baseline DOT data were collected approximately over the right sensorimotor area of ten human subjects (9 male, 1 female, median age 31, 9 right hand dominant, 1 left hand dominant). The subjects were instructed to lie quietly in the dark and to breathe freely. The raw optical measurements were collected with a continuous wave DOT instrument (Franceschini et al., 2003), demodulated and down sampled to 1 Hz. The photon fluence and auxiliary physiological measurements were high-pass-filtered in a forward then reverse direction with a 6th order IIR Butterworth filter with a cutoff frequency of 0.05 Hz and zero phase distortion. This filtering step removes slow physiology that is sufficiently outside the frequency range of interest for the hemodynamic response that it can be ignored. Short-term physiological variability including the respiratory sinus arrhythmia, Mayer waves and vasomotion is still present after filtering. The photon fluence $\Phi(t, \lambda)$ was then converted to a change in optical density ΔOD

$$\Delta\text{OD}(t, \lambda) = \ln \left(\frac{\Phi(t, \lambda)}{\Phi_0(\lambda)} \right), \quad (28)$$

where Φ_0 was the average detected photon fluence and $\Delta\text{OD}(t, \lambda)$ are the measurements \mathbf{y} for the state-space model. The three model inputs contained in \mathbf{u} were the Boolean stimulus time vector, the blood pressure variability (BPV) and heart rate variability (HRV) with normalized variances.

Data from only a single source fiber and three detector locations were included in the analysis. The three detectors were arranged around the source fiber with 3 cm separation between the source and detector fibers and 3 cm between neighboring detector fibers as shown on the right side of Fig. 2. We computed the pathlength submatrix \mathbf{L}_0 with a Monte Carlo simulation of the transport equation (Boas et al., 2002) for a slab model of the scalp, skull, CSF and brain with 1 mm isometric voxels as illustrated on the left side of Fig. 2. Approximate slab thicknesses and tissue optical properties were adapted from Strangman et al. (2003). Given that there are only three detectors, we felt that it was reasonable to use a simple slab model of the tissue. In the present experiment, the anatomical and photon migration models are mathematical placeholders for future work that will explore the effects of complex anatomical structures and larger extent tomography.

We populated the extinction coefficient submatrix \mathbf{E}_0 with values tabulated by Prahl (2005). The spatial basis set matrix \mathbf{G}_0 defines weighted sets of the 1 mm isometric voxels for the analysis. We chose to define three spatial bases with Boolean weights along the boundaries shown in Fig. 2. Basis 1 represents the scalp and is

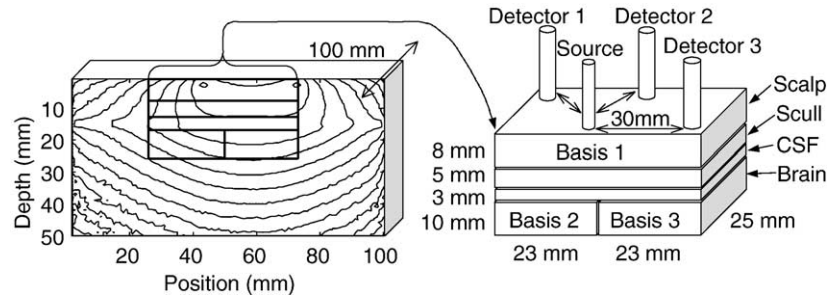


Fig. 2. On the left is shown a slice of the pathlength matrix for detector 3 and 830 nm wavelength light. The contours represent the decay in sensitivity on a logarithmic scale. The boundaries of the spatial basis set contained in \mathbf{G}_0 are shown with bold lines and expanded on the right side of the figure. The arrangement of source and detector fibers is shown relative to the spatial bases and tissue types in the slab model.

common to all the detectors. Bases 2 and 3 represent two regions of the brain located under the scalp basis. Outside of these boundaries, the spatial basis weights were set to zero. The size of the scalp basis is 4.8 cm by 2.4 cm by 0.8 cm thick. The brain bases are both 2.4 cm by 2.4 cm by 0.8 cm thick. We chose to keep the spatial extent of our test case small so that emphasis of the present work is on the physiological modeling aspect of the state-space model rather than the biophysics of photon migration in the head anatomy.

We used a normalized Gaussian function to derive the temporal basis set \mathbf{H}_0 . The standard deviation for the Gaussian function was fixed at 1.5 s, and the means were separated by 1.5 s over the regression time as shown in Fig. 3. The same temporal basis set was used for each input and spatial basis. The states to be estimated by the static or Kalman filter estimators are the stationary or time-varying weights for these temporal bases respectively.

The stimulus paradigm for the simulated cerebral hemodynamics followed an event-related design with a uniformly distributed 12 to 18 s inter-stimulus interval over the 300 s runs. The model used to simulate the functional response was one period of an offset cosine with a delay and amplitude set differently for HbO and HbR. The simulated waveforms can be seen in the results figures.

We specified the simulated functional responses to be localized in basis 2 of the brain. We then propagated the simulated responses through our state-space model to get simulated measurements containing only the functional response from brain basis 2. We then added the simulated measurements to the measurements of real baseline physiology for the 10 human subjects. The variance in the simulated measurements typically equaled 10 to 30% of the physiological variance in the real measurements depending on the subject. Given the average of only 20 stimuli in a run, accurately recovering the functional response from a single run presents a significant signal processing challenge.

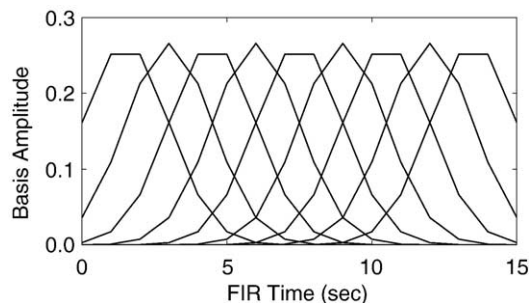


Fig. 3. Temporal basis set specified in \mathbf{H}_0 .

For the static least-squares estimator, we evaluate two cases. In the first case (Static), we only used the Boolean stimulus vector (Stim) as an input \mathbf{u} . This means that the physiological fluctuations are implicitly modeled in the measurement noise \mathbf{v} . In the second case (Physio), we used all three inputs in \mathbf{u} , namely, the stimulus vector (Stim), blood pressure variability (BPV) and heart rate variability (HRV). Since we included BPV and HRV as inputs, the physiological fluctuations from the human subjects were explicitly included in the state-space model. The Tikhonov regularization parameters α for the static estimators were set to maximize the average coefficient of determination R^2 for the estimated functional response.

For the dynamic Kalman filter estimator (Kalman), we again used the stimulus vector, BPV and HRV as inputs \mathbf{u} so the physiology was explicitly modeled. The Kalman filter requires noise and measurement covariance priors. The state update noise covariance \mathbf{Q} only contained nonzero terms on the diagonal elements. Diagonal terms related to the functional response were set to 2.5×10^{-6} , and those related to BPV and HRV were set to 5×10^{-6} . This imbalance in state update noise caused the functional response model to evolve more slowly than the systemic physiological models. The measurement noise covariance matrix \mathbf{R} was set to an identity scaled by 8×10^{-1} . These variances act as regularization and were adjusted to stabilize the estimation scheme and to maximize R^2 for the functional response.

Results

Example results of dynamic physiological modeling for diffuse optical tomography with our proposed state-space model and Kalman filter estimator are shown in Fig. 4. We generated the signal components in the figure by propagating the state estimates $\hat{\mathbf{x}}$ through the state-space model in Fig. 1b until just before the signal enters the summing matrix \mathbf{S} . At this point in the model, the modeled effects of each input in \mathbf{u} on the ΔOD measurements \mathbf{y} are still separated. These modeled measurement components related to each input are shown for subjects 3 and 4 for the 830 nm and 690 nm measurements from detector 1. The example results in Fig. 4 are not intended as validation but rather illustration of how our state-space model can be used to separate measurements into physiological components.

Functional response estimates from spatial basis 2 in the brain (see Fig. 2) for subjects 1 through 4 with the two static estimators (Static and Physio) and the dynamic estimator (Kalman) are shown in Figs. 5, 6 and 7 respectively. When our state-space model and static estimator are used without physiological inputs as shown in

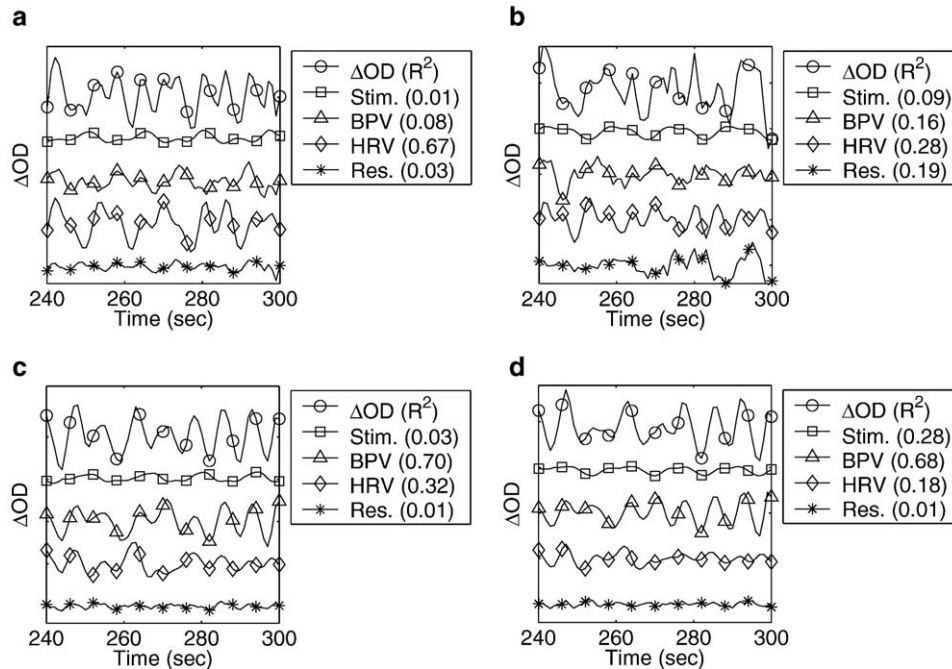


Fig. 4. Dynamic physiological modeling of detector 1 ΔOD measurements into components related to the model inputs. The scale for each component was shifted for visual comparison. The R^2 values in parentheses indicate how much of the ΔOD measurement variance is explained by each modeled component. (a) 830 nm for Subject 3. (b) 690 nm for Subject 3. (c) 830 nm for Subject 4. (d) 690 nm for Subject 4.

Fig. 5, the functional responses are present in the estimates but are distorted by large physiological variation artifacts. Just adding blood pressure variability and heart rate variability as inputs u to the state-space model appears to reduce the physiological variation artifacts in

the functional response estimates and to increase the coefficient of determination R^2 in most cases as shown in Fig. 6. Further improvement in the functional response estimates is apparent when the dynamic Kalman filter estimator is used as shown in Fig. 7. The

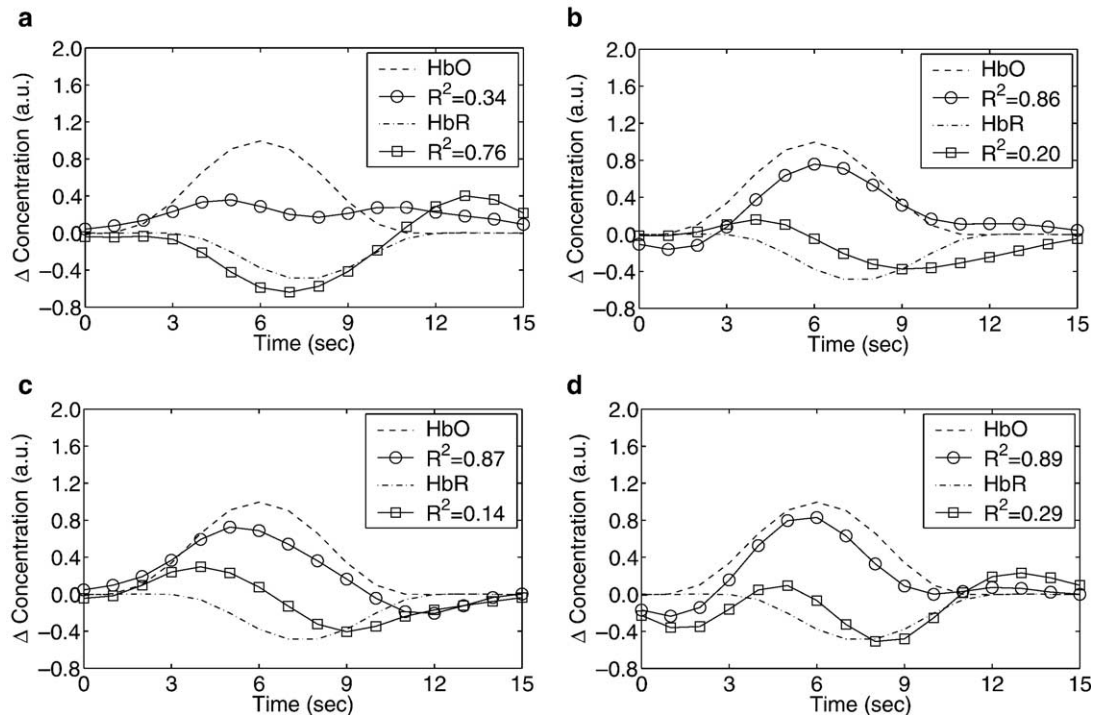


Fig. 5. Functional response estimates from spatial basis 2 in the brain for the static estimator without physiological inputs (Static). The HbO responses are the solid lines marked with circles, and the HbR responses are marked with squares. The R^2 values indicating the goodness of fit with the true hemodynamics (dashed lines) are noted in the legend. (a) Subject 1. (b) Subject 2. (c) Subject 3. (d) Subject 4.

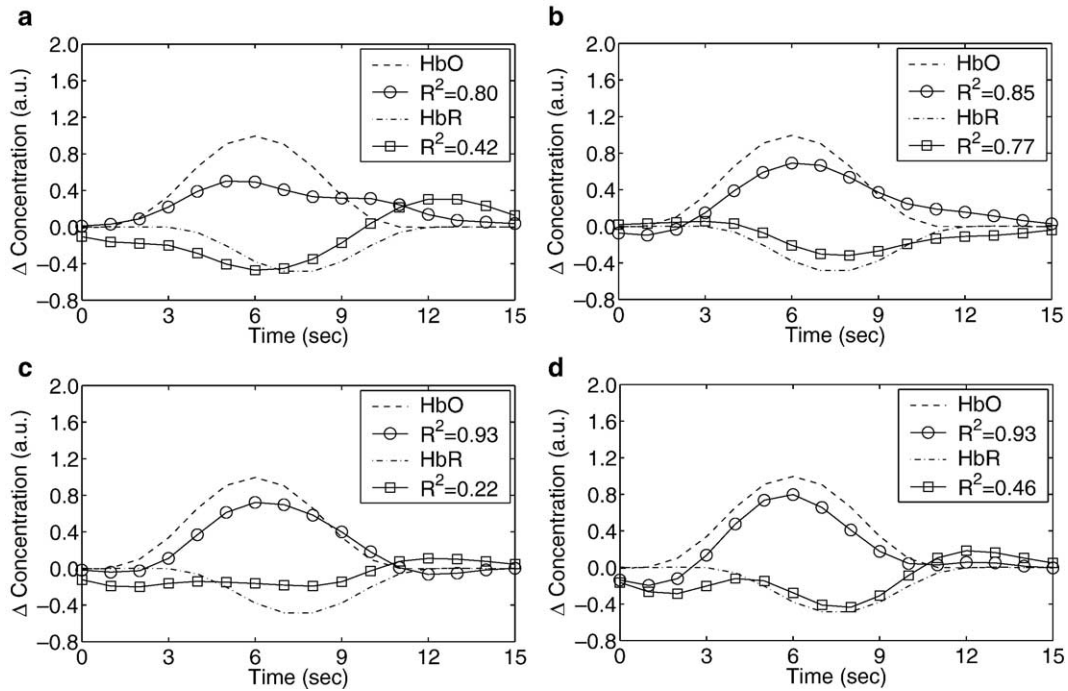


Fig. 6. Functional response estimates from spatial basis 2 in the brain for the static estimator with physiological inputs (Physio). HbO and HbR estimates are marked with circles and squares respectively. True hemodynamics are dashed lines, and R^2 values are marked in the figure legend. (a) Subject 1. (b) Subject 2. (c) Subject 3. (d) Subject 4.

attenuation of the functional response estimate amplitudes results from the need for regularization with all the estimators.

The R^2 coefficients comparing the estimated functional response in HbO and HbR to the true responses for all subjects are summarized in Fig. 8. We used the Fisher Z transformation on

the correlation coefficients from each regression so that the values took on an approximate normal distribution. The mean and standard deviation was computed from the Z values, and the result was inverse transformed back to R values then squared. Paired t tests were then performed on the Z values between all pairs of

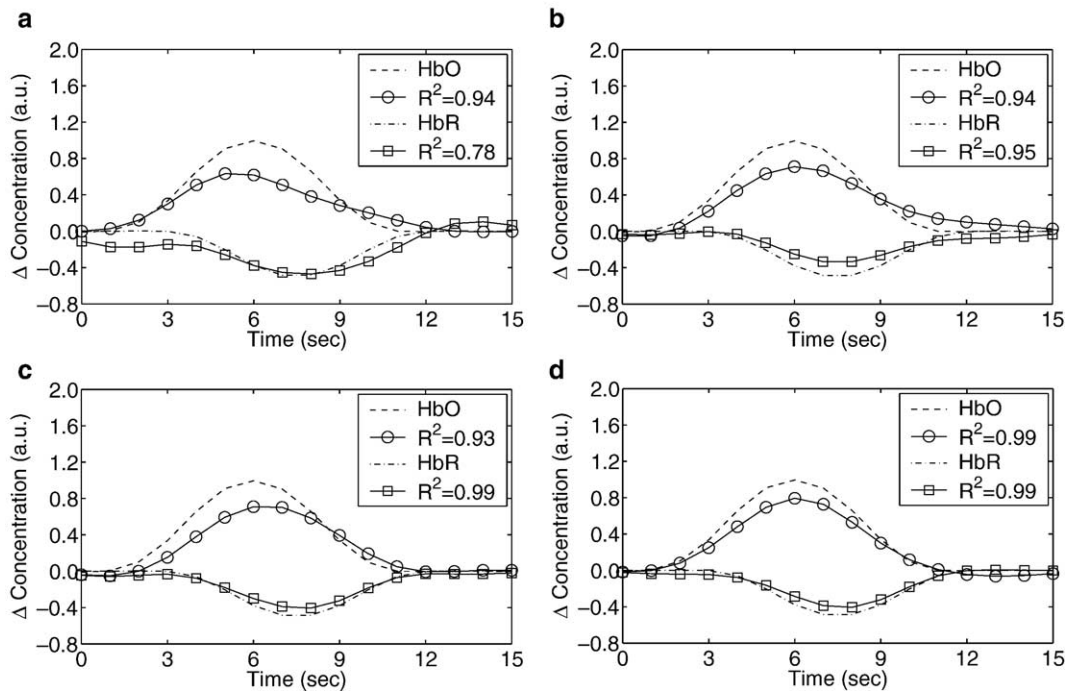


Fig. 7. Functional response estimates from spatial basis 2 in the brain for the dynamic Kalman filter estimator with physiological inputs (Kalman). HbO and HbR estimates are marked with circles and squares respectively. True hemodynamics are dashed lines, and R^2 values are marked in the figure legend. (a) Subject 1. (b) Subject 2. (c) Subject 3. (d) Subject 4.

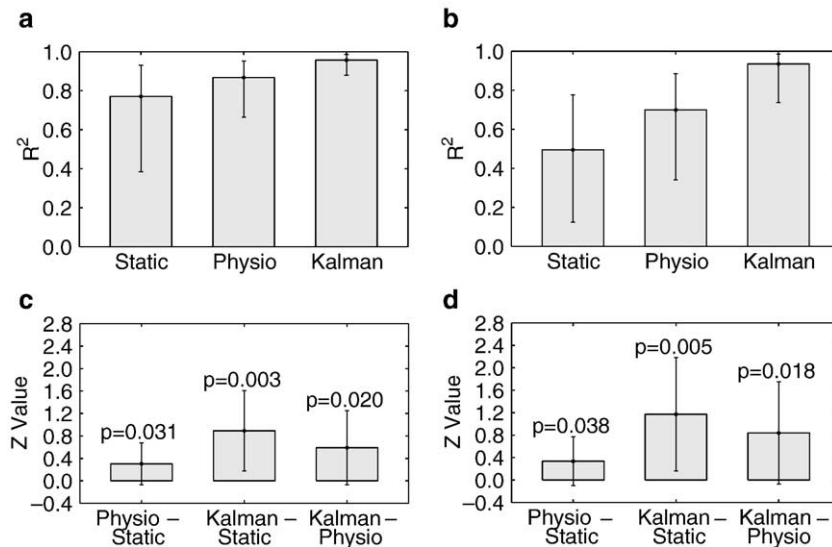


Fig. 8. Coefficients of determination (R^2) for functional response estimates from spatial basis 2 in the brain for the static estimator without (Static) and with (Physio) physiological inputs and for the dynamic Kalman filter estimator with physiological inputs (Kalman). The error bars indicate standard deviation. The significance of differences was tested with a two-tailed paired t test, and resulting P values are indicated. (a) R^2 values for HbO. (b) R^2 values for HbR. (c) Paired Differences for HbO. (d) Paired Differences for HbR.

estimators (Physio-Static, Kalman-Static and Kalman-Physio). The null hypothesis was that there was no difference between the Z values. The R^2 values were found to be significantly improved ($n = 10$, $P < 0.05$) when physiological inputs were used with the static estimator. The Kalman filter estimates were significantly better than either of the static estimator cases.

The average measurement variance explained by the model components related to each input for the two static estimator cases (Static and Physio) and the dynamic estimator case (Kalman) are summarized in Fig. 9. The measurement components and coefficients of determination R^2 were obtained in the same way as those shown in Fig. 4. Averages were computed after applying the Fisher Z transformation, and the result was inverse transformed. Although the inter-subject variability was large, blood pressure and heart rate variability consistently accounted for a major portion of the measurement variance when included as inputs (Physio and Kalman). The differences in the variance explained by the residual for the three estimation cases were all highly significant (two-tailed, paired t test, $n = 10$, $P < 0.001$). The variance explained by the BPV component of the measurements was just significant at the $P < 0.05$ level for the 830 nm measurements and approached significance at $P = 0.053$ for the 690 nm measurements (two-tailed, paired t test, $n = 10$). Other differences in R^2 were not significant.

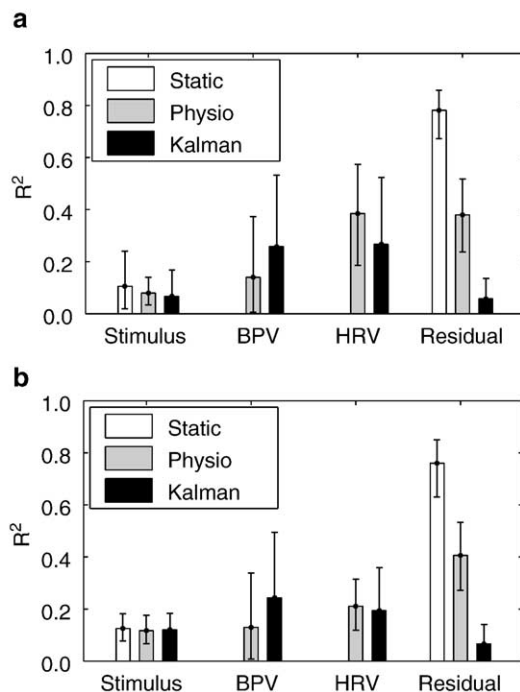


Fig. 9. Measurement variance explained by modeled components related to inputs u . Results are from the static estimator cases without (Static) and with physiological inputs (Physio) and the dynamic Kalman filter estimator with physiological inputs (Kalman). The mean and standard deviation error bars were computed as Fisher transformed Z values. (a) 830 nm. (b) 690 nm.

Discussion

Static versus dynamic filtering of physiological interference

We initially hypothesized that including systemic physiological inputs in the state-space model analysis would improve estimates of the functional hemodynamic response function (HRF) and that the dynamic Kalman filter approach would offer further improvement. This hypothesis is supported in fMRI analysis where physiological filters are sometimes added to the general linear model to remove physiological interference (Worsley and Friston, 1995; Purdon and Weisskoff, 1998). The details of how the physiological filtering is performed vary widely from sinusoidal regressors (Josephs et al., 1997) to spatiotemporal modeling (Purdon et al., 2001). Dynamic methods have also found good success in fMRI analysis but again with a wide range of methods. Friston (2002) applies Bayesian estimation methods to dynamically

model fMRI. Gössl et al. (2000) use a nonparametric estimate of the baseline variability and estimation of time-varying effects of stimulation. Riera et al. (2004) applies a state-space method that includes nonlinear hemodynamic models and physiological noise. Despite the variations in method, these fMRI studies all support the notion that dynamic analysis provides superior estimates of the HRF than time-invariant methods. Kolehmainen et al. (2003) offer the first example of a dynamic state-space approach to DOT analysis, but the formulation does not include any physiological interference. Prince et al. (2003) were the first to dynamically model physiological interference in DOT, but no comparisons are made with static methods. The present study is the first to quantitatively evaluate dynamic and static filtering of physiological interference by combining real physiological interference with a simulated functional response.

The results of the present study are consistent with our hypothesis that physiological modeling improves HRF estimates in DOT. Although the HRF component of the data in our validation study was simulated, the physiological interference shown in the estimates of Fig. 5 typify what we observe experimentally with response estimates to finger tapping. The reduction in interference achieved by including physiological inputs in the model is apparent in Fig. 6, and this improvement is reflected in the average goodness of fit reported in Fig. 8. The R^2 values are generally greater for HbO than for HbR, which is expected given that blood volume fluctuations are larger in the arteries. The greater challenge of estimating the HbR response also appears to provide more room for improvement with our dynamic physiological modeling. Improved HRF estimates may be achieved here because the physiological modeling accounts for some of the measurement variance as shown in Fig. 9, and so less interference remains that might correlate with the stimulus. We anticipate that, with real experimental stimulus data, the systemic physiology may also respond to the stimulus (e.g. heart rate increases with physical activity). In such a case, we expect that including the physiological inputs in the model will help to reduce false-positive functional responses in the brain. We plan to test this hypothesis in future studies.

The present study also supports our hypothesis that dynamic physiological modeling is superior to static modeling as reflected in the HRF estimates shown in Fig. 7. The further increase in average R^2 shown in Fig. 8 represents the improvement with dynamic modeling. In our validation, we did not consider that the functional response may not be identical from every repeated stimulus. It is known from fMRI that a degree of variance exists in the hemodynamic response within an experiment (Miezin et al., 2000). Dynamic estimation methods should be inherently superior when this nonstationarity is present in the data. There are also a number of improvements that could be made to the dynamic estimation methods as they are applied in this study. The areas for improvement include adding a reversed time direction Kalman smoother, better covariance estimates for the state evolution and possibly an alternate, more robust, dynamic state-space estimator.

Prior information in DOT

Spatial priors

Tomographic reconstructions for DOT are challenging from a statistical and computational standpoint. Under most experimental conditions, the number of voxels exceeds the number of measurements by 1 or 2 orders of magnitude, making the inverse problem highly under defined. The diffuse nature of photon propagation in

the tissue also results in a poorly conditioned inverse problem particularly with respect to depth resolution. A number of authors have proposed methods of incorporating prior information into the tomography problem to improve image reconstructions. Schweiger et al. (2005) and Pogue et al. (1999) describe spatial regularization approaches that reduce spatial variance in exchange for increased model residual. Applying a cortical constraint to the reconstructions has also been described by Pogue and Paulsen (1998) and Boas and Dale (2005). Another approach is to define a functional region of interest (ROI) based on prior knowledge of the anatomy (Zhang et al., 2005a; Gibson et al., 2005b).

In the proposed Kalman filter framework, a spatial basis set must be specified, but its form is not prescribed. This flexibility in defining the spatial basis set permits inclusion of spatial regularization by defining the bases as overlapping smoothing kernels, which is a commonly used spatial smoothing approach in fMRI (Friston et al., 2000a). The bases could also be bounded by anatomical or functional regions to implement cortical or ROI priors. In the present validation experiment, large spatial basis functions were used to match the number of effective voxels to the number of measurements to avoid the under defined problem. We structured our experiment in this way to shift the focus from spatial to temporal modeling while leaving the mathematical structure for larger scale tomography intact for further study in the future. It will be necessary to significantly increase the number of measurements and to have overlapping measurements to properly explore the effects of spatial priors on the dynamic DOT inverse problem.

Spectral priors

Specifying the chromophores present in the tissue and their optical properties constitutes a spectral prior. Wavelength-dependent extinction coefficients for the chromophores are readily available in the literature (Prahl, 2005). The advantage of using spectral priors is that the concentrations of multiple chromophores can be estimated as described by Cope et al. (1991). Systematic errors in chromophore concentrations, referred to as cross talk, can arise due to pathlength uncertainties (Strangman et al., 2003; Uludag et al., 2002). Regularizing the inversion, including more wavelengths than the number of chromophores, and careful selection of wavelengths as described by Corlu et al. (2005) all help to reduce the cross-talk problem. The present framework includes an extinction coefficient matrix \mathbf{E}_0 for inclusion of spectral priors without any limitations on the number of wavelengths or chromophores.

Temporal priors

Temporal priors include everything from hemodynamic models of the neurovascular response such as the gamma function often used in fMRI (Friston et al., 1998) to nonlinear models of the vascular dynamics like the balloon model (Buxton et al., 1998; Friston et al., 2000b; Mandeville et al., 1999). Even deconvolution methods implicitly bound the duration of the impulse response (Josephs et al., 1997). This is a challenging area because accurate models are generally too complex and nonlinear to be solved as an inverse problem. Models that are numerically tractable inverse problems typically have ad hoc elements that make physiological interpretation more difficult. In the proposed framework, the temporal model is a dynamic, causal FIR transfer function for each input-spatial basis combination. The FIR transfer function is constructed from a temporal basis set again without prescribing its form. The temporal smoothness of the FIR functions can be assumed by using, for example, an overlapping Gaussian basis set

as in the present experiment. Even more constraints can be added using an assumed time course for the hemodynamic response for the basis set as described by Zhang et al. (2005c).

In a dynamic estimation framework, another category of temporal priors is included that constrains the temporal evolution of the states. In the present formulation, the states evolve as random processes with a covariance prior. We used this covariance prior to allow the BPV and HRV models to evolve more rapidly than the functional response model. This had the effect of drawing more of the random variance away from the functional response model and improved the R^2 values for the functional hemodynamics and illustrates how priors are sometimes used as regularization parameters. Some technical aspects of the dynamic priors in the proposed Kalman filter framework could be more sophisticated. We manually tuned the process noise covariance, but there are automatic tuning procedures in the literature that may be appropriate for this application (Kitagawa, 1998). Future implementations should also include a state estimate smoother that operates in a reversed time direction as described by Kaipio and Somersalo (2004). This will help remove any lag in the state estimates and reduce the random variance in the temporal evolution of the states.

Covariance between spatial, spectral and temporal priors

Additional benefit from prior information can be obtained by modeling the co-variance between multiple priors. The benefits of combined spatial and spectral priors have been demonstrated previously (Li et al., 2005; Pogue and Paulsen, 1998). Zhang et al. (2005c) combined spatial, spectral and temporal priors but only with a time-invariant system model. In the proposed state-space model, covariances between the spatial, spectral and temporal priors are all included. We expect these covariances to improve the tomographic reconstructions including possibly increased depth resolution.

Anatomical and physiological models

Comprehensive DOT data analysis requires a biophysical model of all the relevant anatomy and physiology formulated as a numerically tractable inverse problem. Koyama et al. (2005) and Boas et al. (2002) describe how DOT interacts with the anatomical structure of the human head. Anatomical MRI is a useful prior for DOT analysis (Barbour et al., 1995; Pogue and Paulsen, 1998; Boas and Dale, 2005). DOT reveals the physiological dynamics in hemoglobin concentration in the scalp and in the brain. Unraveling these dynamics is a nontrivial inverse problem. A significant advantage of a dynamic state-space approach for DOT analysis is that it is particularly suitable to this class of inverse problems. Arnold et al. (1998) provide an example of dynamic state-space modeling of cardiac and respiratory interactions in the electroencephalogram (EEG).

If nonlinear models are used, then the extended Kalman filter is an alternate formulation that facilitates dynamic parameter estimation (Kailath et al., 2000). This research direction could extend to integrating systems-level or large-scale neural modeling (Horwitz et al., 1999) or dynamic causal modeling (Friston et al., 2003) with the biophysics of DOT into a comprehensive inverse problem formulation. Nonlinear circuit models are available to describe the cardiovascular system (Mukkamala and Cohen, 2001), cerebral autoregulation and gas exchange (Lu et al., 2003), vasomotion (Ursino et al., 1998) and functional hemodynamics (Friston et al., 2000b). A natural extension of this physiological modeling strategy

is to relate the biophysics of multiple imaging modalities that can be performed simultaneously, such as DOT, EEG and fMRI, to a common anatomical and physiological model. The physiologically relevant parameters would then be estimated in a dynamic state-space formulation.

Physiologically based interpretations of the neuroimaging data offer advantages to neuroscience advancement and clinical applications. Identifying mechanical properties of the cerebral vasculature, for example, could help to diagnose neurovascular pathologies like those found in Alzheimer's disease. Simultaneous fMRI and DOT may help to illuminate the physiological dynamics of neurovascular coupling that are the basis of hemodynamic neuroimaging (Buxton et al., 1998; Friston et al., 2000b; Mandeville et al., 1999). We designed the present state-space model as a first step toward physiological interpretation of DOT and multimodal integration.

Extending to larger dimensional reconstruction

One of the practical challenges of dynamic state-space analysis in DOT and other functional imaging technologies is the large dimensionality of the data and analysis models. In the formulation by Gössl et al. (2000), there are as many parameters to estimate as there are observations for one effect. Large scale state-space estimation is not a new challenge but is still an active area of research. Khellah et al. (2005) provide an example of a new large-scale technique from geophysics. The reduced rank square root implementations of the Kalman filter are a notable method for estimating otherwise unfeasibly large problems (Verlaan and Heemink, 1997).

Although the proposed state-space approach was evaluated with only a small spatial basis set, the same framework can be used for problems of much larger spatial extent. The focus of the present experiment was the temporal system identification aspect of DOT; the spatial aspect will be examined in subsequent investigations. Spatially overlapping and multi-distance measurements are also desirable to fully utilize the tomography mathematics. Toward this aim, the proposed state-space approach will accommodate time domain multiplexing of the measurements (Boas et al., 2004a; Bluestone et al., 2001), which is a requirement for collecting measurements from source–detector separations that exceed the limited dynamic range for the instrumentation. While dynamically adjusting the detector gains permits an effective expansion of the dynamic range, temporal gaps occur in the measurements. An advantage of the proposed state-space model and Kalman filter estimator is that these gaps in the data should be well tolerated.

Conclusion

Our state-space model for DOT analysis is purposefully versatile, and so its implementation requires specification of certain model elements. We frame a series of questions here as a guide to using the proposed model. *Who?* Determine which physiological and experimental inputs are important for the analysis. *Where?* Specify the spatial basis set and photon pathlength matrix for the anatomical structure. *When?* Specify the temporal basis set for the finite impulse response models. *What?* Estimate the states in the model. *How?* Determine how the modeled components are related to functional anatomy and physiology. *Why?* Hypothesize why the functional anatomy and physiology is related to the model inputs.

The present work is only a step toward a comprehensive dynamic framework for DOT data analysis and interpretation. The proposed dynamic state-space approach has the potential to significantly improve estimates of functional hemodynamics in DOT neuroimaging and may open the door to a broader range of brain activation paradigms. The ability to separate signals into physiological components may reveal new information about the local regulatory physiology and may be useful in identifying certain vascular pathologies. Unlike the prior work with the Kalman filter for DOT, the present formulation has the flexibility to be applied to any experimental design and a broad range of spatial, spectral and temporal priors. The proposed Kalman filter framework may also be useful for other imaging modalities such as fMRI, MEG and EEG or when multiple modalities are combined with a single state-space model of the underlying physiology.

Acknowledgments

This work was supported by NIH T32-CA09502, P41-RR14075, R01-EB001954 and the MIND Institute. The authors would like to thank Professor Dana H. Brooks, Ph.D. of Northeastern University for reviewing the manuscript and providing insightful feedback.

References

- Adelson, P.D., Nemoto, E., Scheuer, M., Painter, M., Morgan, J., Yonas, H., 1999. Noninvasive continuous monitoring of cerebral oxygenation periodically using near-infrared spectroscopy: a preliminary report. *Epilepsia* 40, 1484–1489.
- Arnold, M., Miltner, W.H.R., Witte, H., Bauer, R., Braun, C., 1998. Adaptive AR modeling of nonstationary time series by means of Kalman filtering. *IEEE Trans. Biomed. Eng.* 45 (5), 553–562.
- Arridge, S.R., 1999. Optical tomography in medical imaging. *Inverse Probl.* 15, R41–R93.
- Arridge, S.R., Cope, M., Delpy, D.T., 1992. The theoretical basis for the determination of optical pathlengths in tissue: temporal and frequency analysis. *Phys. Med. Biol.* 37, 1531–1560.
- Baird, A.A., Kagan, J., Gaudette, T., Walz, K.A., Hershlag, N., Boas, D.A., 2002. Frontal lobe activation during object permanence: data from near-infrared spectroscopy. *NeuroImage* 16, 1120–1126.
- Barbour, R.L., Graber, H.L., Chang, J., Barbour, S.S., Koo, P.C., Aronson, R., 1995. MRI-guided optical tomography: prospects and computation for a new imaging method. *IEEE Comput. Sci. Eng.* 2, 63–77.
- Bluestone, A., Abdoulaev, G., Schmitz, C., Barbour, R., Hielscher, A., 2001. Three-dimensional optical tomography of hemodynamics in the human head. *Opt. Express* 9, 272–286.
- Boas, D.A., Dale, A.M., 2005. Simulation study of magnetic resonance imaging-guided cortically constrained diffuse optical tomography of human brain function. *Appl. Opt.* 44 (10), 1957–1968.
- Boas, D.A., Culver, J., Scott, J., Dunn, A.K., 2002. Three dimensional Monte Carlo code for photon migration through complex heterogeneous media including the adult head. *Opt. Express* 10, 159–170.
- Boas, D.A., Chen, K., Grebert, D., Franceschini, M.A., 2004a. Improving diffuse optical imaging spatial resolution of cerebral hemodynamic response to brain activation in humans. *Opt. Lett.* 29, 1506–1508.
- Boas, D.A., Dale, A.M., Franceschini, M.A., 2004b. Diffuse optical imaging of brain activation: approaches to optimizing image sensitivity, resolution and accuracy. *NeuroImage* 23, S275–S288.
- Buxton, R.B., Wong, E.C., Frank, L.R., 1998. Dynamics of blood flow and oxygenation changes during brain activation: the balloon model. *Magn. Reson. Med.* 39 (6), 855–864.
- Chandrasekhar, S., 1960. *Radiative Transport*. Dover, New York.
- Chen, W.G., Li, P.C., Luo, Q.M., Zeng, S.Q., Hu, B., 2000. Hemodynamic assessment of ischemic stroke with near-infrared spectroscopy. *Space Med. Med. Eng. (Beijing)* 13, 84–89.
- Chen, S., Sakatani, K., Lichty, W., Ning, P., Zhao, S., Zuo, H., 2002. Auditory-evoked cerebral oxygenation changes in hypoxic–ischemic encephalopathy of newborn infants monitored by near infrared spectroscopy. *Early Hum. Dev.* 67, 113–121.
- Cohen, M.A., Taylor, J.A., 2002. Short-term cardiovascular oscillations in man: measuring and modelling the physiologies. *J. Physiol.* 542 (Pt. 3), 669–683.
- Colier, W.N., Quaresima, V., Oeseburg, B., Ferrari, M., 1999. Human motor-cortex oxygenation changes induced by cyclic coupled movements of hand and foot. *Exp. Brain Res.* 129, 457–461.
- Cope, M., van der Zee, P., Essenpreis, M., Arridge, S.R., Delpy, D.T., 1991. Data analysis methods for near infrared spectroscopy of tissue: problems in determining the relative cytochrome aa3 concentration. *SPIE* 1431, 251–262.
- Corlu, A., Choe, R., Durduran, T., Lee, K., Schweiger, M., Arridge, S.R., Hillman, E.M.C., Yodh, A.G., 2005. Diffuse optical tomography with spectral constraints and wavelength optimization. *Appl. Opt.* 44 (11), 2082–2093.
- Dehghani, H., Pogue, B.W., Poplack, S.P., Paulsen, K.D., 2003. Multi-wavelength three-dimensional near-infrared tomography of the breast: initial simulation, phantom, and clinical results. *Appl. Opt.* 42 (1), 135–145.
- Eschweiler, G.W., Wegerer, C., Schlotter, W., Spandl, C., Stevens, A., Bartels, M., Buchkremer, G., 2000. Left prefrontal activation predicts therapeutic effects of repetitive transcranial magnetic stimulation (rTMS) in major depression. *Psychiatry Res.* 99, 161–172.
- Fallgatter, A.J., Strik, W.K., 2000. Reduced frontal functional asymmetry in schizophrenia during a cued continuous performance test assessed with near-infrared spectroscopy. *Schizophr. Bull.* 26, 913–919.
- Fallgatter, A.J., Roesler, M., Sitzmann, L., Heidrich, A., Mueller, T.J., Strik, W.K., 1997. Loss of functional hemispheric asymmetry in Alzheimer's dementia assessed with near-infrared spectroscopy. *Brain Res. Cogn. Brain Res.* 6, 67–72.
- Frackowiak, R.S.J., Friston, K.J., Frith, C., Dolan, R., Price, C.J., Zeki, S., Ashburner, J., Penny, W.D. (Eds.), 2003. *Human Brain Function*, 2nd ed. Academic Press. URL <http://www.fil.ion.ucl.ac.uk/spm/doc/books/hbf2/>.
- Franceschini, M.A., Fantini, S., Thompson, J.H., Culver, J.P., Boas, D.A., 2003. Hemodynamic evoked response of the sensorimotor cortex measured non-invasively with near-infrared optical imaging. *Psychophysiology* 40, 548–560.
- Friston, K.J., 2002. Bayesian estimation of dynamical systems: an application to fMRI. *NeuroImage* 16, 513–530.
- Friston, K.J., Fletcher, P., Josephs, O., Holmes, A., Rugg, M.D., Turner, R., 1998. Event-related fMRI: characterizing differential responses. *NeuroImage* 7, 30–40.
- Friston, K.J., Josephs, O., Zarahn, E., Holmes, A.P., Rouquette, S., Poline, J.B., 2000a. To smooth or not to smooth? Bias and efficiency in fMRI time-series analysis. *NeuroImage* 12 (2), 196–208.
- Friston, K.J., Mechelli, A., Turner, R., Price, C.J., 2000b. Nonlinear responses in fMRI: the Balloon model, Volterra kernels, and other hemodynamics. *NeuroImage* 12 (4), 466–477.
- Friston, K.J., Harrison, L., Penny, W., 2003. Dynamic causal modelling. *NeuroImage* 19 (4), 1273–1302.
- Fukui, Y., Ajichi, Y., Okada, E., 2003. Monte Carlo prediction of near-infrared light propagation in realistic adult and neonatal head models. *Appl. Opt.* 42 (16), 2881–2887.
- Gibson, A.P., Hebden, J.C., Arridge, S.R., 2005a. Recent advances in diffuse optical imaging. *Phys. Med. Biol.* 50, R1–R43.
- Gibson, A.P., Hebden, J.C., Riley, J., Everdell, N., Schweiger, M., Arridge, S.R., Delpy, D.T., 2005b. Linear and nonlinear reconstruction for optical tomography of phantoms with nonscattering regions. *Appl. Opt.* 44 (19), 3925–3936.

- Gössl, C., Auer, D.P., Fahrmeir, L., 2000. Dynamic models in fMRI. *Magn. Reson. Med.* 43, 72–81.
- Goutte, C., Nielsen, F.A., Hansen, L.K., 2000. Modeling the haemodynamic response in fMRI using smooth FIR filters. *IEEE Trans. Med. Imag.* 19 (12), 1188–1201.
- Hanlon, E.B., Itzkan, I., Dasari, R.R., Feld, M.S., Ferrante, R.J., McKee, A.C., Lathi, D., Kowall, N.W., 1999. Near-infrared fluorescence spectroscopy detects Alzheimer's disease in vitro. *Photochem. Photobiol.* 70, 236–242.
- Hayashi, T., Kashio, Y., Okada, E., 2003. Hybrid Monte Carlo-diffusion method for light propagation in tissue with a low-scattering region. *Appl. Opt.* 42 (16), 2888–2896.
- Hebden, J.C., Gibson, A., Austin, T., Yusof, R.M., Everdell, N., Delpy, D.T., Arridge, S.R., Meek, J.H., Wyatt, J.S., 2004. Imaging changes in blood volume and oxygenation in the newborn infant brain using three-dimensional optical tomography. *Phys. Med. Biol.* 49 (7), 1117–1130.
- Hintz, S.R., Benaron, D.A., Siegel, A.M., Zourabian, A., Stevenson, D.K., Boas, D.A., 2001. Bedside functional imaging of the premature infant brain during passive motor activation. *J. Perinat. Med.* 29 (4), 335–343.
- Hock, C., Villringer, K., Müller-Spahn, F., Hofmann, M., Schuh-Hofer, S., Heekeren, H., Wenzel, R., Dirnagl, U., Villringer, A., 1996. Near infrared spectroscopy in the diagnosis of Alzheimer's disease. *Ann. N. Y. Acad. Sci.* 777, 22–29.
- Horwitz, B., Tagamets, M.A., McIntosh, A.R., 1999. Neural modeling, functional brain imaging, and cognition. *Trends Cogn. Sci.* 3 (3), 91–98.
- Jakubowski, D.B., Cerussi, A.E., Bevilacqua, F., Shah, N., Hsiang, D., Butler, J., Tromberg, B.J., 2004. Monitoring neoadjuvant chemotherapy in breast cancer using quantitative diffuse optical spectroscopy: a case study. *J. Biomed. Opt.* 9 (1), 230–238.
- Josephs, O., Turner, R., Friston, K., 1997. Event-related fMRI. *Hum. Brain Mapp.* 5 (4), 243–248.
- Kailath, T., Sayed, A.H., Hassibi, B., 2000. *Linear estimation. Information and System Sciences.* Prentice-Hall.
- Kaipio, J.P., Somersalo, E., 2004. *Statistical and Computational Inverse Problems, Applied Mathematical Sciences*, vol. 160. Springer-Verlag.
- Kalman, R.E., 1960. A new approach to linear filtering and prediction problems. *Trans. ASME—J. Basic Eng.* 82, 35–45.
- Kay, S.M., 1993. *Fundamentals of Statistical Signal Processing, Estimation Theory.* Prentice Hall.
- Khellah, F., Fieguth, P., Murray, M.J., Allen, M., 2005. Statistical processing of large image sequences. *IEEE Trans. Image Process.* 14 (1), 80–93.
- Kitagawa, G., 1998. A self-organizing state-space model. *J. Am. Stat. Assoc.* 93 (443), 1203–1215.
- Kolehmainen, V., Prince, S., Arridge, S., Kaipio, J., 2003. State-estimation approach to the nonstationary optical tomography problem. *J. Opt. Soc. Am. A* 20 (5), 876–889.
- Koyama, T., Iwasaki, A., Ogoshi, Y., Okada, E., 2005. Practical and adequate approach to modeling light propagation in an adult head with low-scattering regions by use of diffusion theory. *Appl. Opt.* 44 (11), 2094–2103.
- Li, A., Boverman, G., Zhang, Y., Brooks, D., Miller, E.L., Kilmer, M.E., Zhang, Q., Hillman, E.M.C., Boas, D.A., 2005. Optimal linear inverse solution with multiple priors in diffuse optical tomography. *Appl. Opt.* 44 (10), 1948–1956.
- Logothetis, N.K., Pauls, J., Augath, M., Trinath, T., Oeltermann, A., 2001. Neurophysiological investigation of the basis of the fMRI signal. *Nature* 412 (6843), 150–157.
- Lu, K., Clark Jr., J.W., Ghorbel, F.H., Ware, D.L., Zwischenberger, J.B., Bidani, A., 2003. Whole-body gas exchange in human predicted by a cardiopulmonary model. *Cardiovasc. Eng. Int. J.* 3 (1), 1–19.
- Lu, K., Clark Jr., J.W., Ghorbel, F.H., Robertson, C.S., Ware, D.L., Zwischenberger, J.B., Bidani, A., 2004. Cerebral autoregulation and gas exchange studied using a human cardiopulmonary model. *Am. J. Physiol.: Heart Circ. Physiol.* 286, H584–H601.
- Mandeville, J.B., Marota, J.J., Ayata, C., Zaharchuk, G., Moskowitz, M.A., Rosen, B.R., Weisskoff, R.M., 1999. Evidence of a cerebrovascular postarteriole windkessel with delayed compliance. *J. Cereb. Blood Flow Metab.* 19 (6), 679–689.
- Matsuo, K., Kato, T., Fukuda, M., Kato, N., 2000. Alteration of hemoglobin oxygenation in the frontal region in elderly depressed patients as measured by near-infrared spectroscopy. *J. Neuropsychiatry Clin. Neurosci.* 12, 465–471.
- Mayhew, J.E.W., Askew, S., Zheng, Y., Porrill, J., Westby, G.W.M., Redgrave, P., Rector, D.M., Harper, R.M., 1996. Cerebral vasomotion: a 0.1-Hz oscillation in reflected light imaging of neural activity. *NeuroImage* 4, 183–193.
- Meek, J.H., Elwell, C.E., McCormick, D.C., Edwards, A.D., Townsend, J.P., Steward, A.L., Wyatt, J.S., 1999. Abnormal cerebral haemodynamics in perinatally asphyxiated neonates related to outcome. *Arch. Dis. Child.* 81, F110–F115.
- Miezin, F.M., Maccotta, L., Ollinger, J.M., Petersen, S.E., Buckner, R.L., 2000. Characterizing the hemodynamic response: effects of presentation rate, sampling procedure, and the possibility of ordering brain activity based on relative timing. *NeuroImage* 11 (6), 735–759 (Part 1).
- Mukkamala, R., Cohen, R.J., 2001. A forward model-based validation of cardiovascular system identification. *Am. J. Physiol.: Heart Circ. Physiol.* 281, H2714–H2730.
- Nemoto, E.M., Yonas, H., Kassam, A., 2000. Clinical experience with cerebral oximetry in stroke and cardiac arrest. *Crit. Care Med.* 28, 1052–1054.
- Obrig, H., Neufang, M., Wenzel, R., Kohl, M., Steinbrink, J., Einhaupl, K., Villringer, A., 2000. Spontaneous low frequency oscillations of cerebral hemodynamics and metabolism in human adults. *NeuroImage* 12 (6), 623–639.
- Okada, F., Tokumitsu, Y., Hoshi, Y., Tamura, M., 1994. Impaired interhemispheric integration in brain oxygenation and hemodynamics in schizophrenia. *Eur. Arch. Psychiatry Clin. Neurosci.* 244, 17–25.
- Okada, E., Schweiger, M., Arridge, S.R., Firbank, M., Delpy, D.T., 1996a. Experimental validation of Monte Carlo and finite-element methods of estimation of the optical path length in inhomogeneous tissue. *Appl. Opt.* 35 (19), 3362–3371.
- Okada, F., Takahashi, N., Tokumitsu, Y., 1996b. Dominance of the 'nondominant' hemisphere in depression. *J. Affective Disord.* 37, 13–21.
- Panerai, R.B., 2004. System identification of human cerebral blood flow regulatory mechanisms. *Cardiovasc. Eng. Int. J.* 4 (1), 59–71.
- Pena, M., Maki, A., Kovacic, D., Dehaene-Lambertz, G., Koizumi, H., Bouquet, F., Mehler, J., 2003. Sounds and silence: an optical topography study of language recognition at birth. *Proc. Natl. Acad. Sci.* 100, 11702–11705.
- Pogue, B.W., Paulsen, K.D., 1998. High-resolution near-infrared tomographic imaging simulations of the rat cranium by use of a priori magnetic resonance imaging structural information. *Opt. Lett.* 23, 1716–1718.
- Pogue, B.W., McBride, T.O., Prewitt, J., Osterberg, U.L., Paulsen, K.D., 1999. Spatially variant regularization improves diffuse optical tomography. *Appl. Opt.* 38, 2950–2961.
- Prahl, S., 2005. Tabulated molar extinction coefficient for hemoglobin in water. Oregon Medical Laser Center. URL <http://omlc.ogi.edu/spectra/hemoglobin/summary.html>.
- Prince, S., Kolehmainen, V., Kaipio, J.P., Franceschini, M.A., Boas, D.A., Arridge, S.R., 2003. Time-series estimation of biological factors in optical diffusion tomography. *Phys. Med. Biol.* 48, 1491–1504.
- Purdon, P.L., Weisskoff, R.M., 1998. Effect of temporal autocorrelation due to physiological noise and stimulus paradigm on voxel-level false-positive rates in fMRI. *Hum. Brain Mapp.* 6 (4), 239–249.
- Purdon, P.L., Solo, V., Weisskoff, R.M., Brown, E.N., 2001. Locally regularized spatiotemporal modeling and model comparison for functional MRI. *NeuroImage* 14 (4), 912–923.
- Riera, J.J., Watanabe, J., Kazuki, I., Naoki, M., Aubert, E., Ozaki, T.,

- Kawashima, R., 2004. A state-space model of the hemodynamic approach: nonlinear filtering of BOLD signals. *NeuroImage* 21, 547–567.
- Ripoll, J., Arridge, S.R., Nieto-Vesperinas, M., 2001. Effect of roughness in non-diffusive regions within diffusive media. *J. Opt. Soc. Am. A* 18, 940–947.
- Rostrup, E., Law, I., Pott, F., Ide, K., Knudsen, G.M., 2002. Cerebral hemodynamics measured with simultaneous PET and near-infrared spectroscopy in humans. *Brain Res.* 954 (2), 183–193.
- Ruben, J., Wenzel, R., Obrig, H., Villringer, K., Bernarding, J., Hirth, C., Heekeren, H., Dirnagl, U., Villringer, A., 1997. Haemoglobin oxygenation changes during visual stimulation in the occipital cortex. *Adv. Exp. Med. Biol.* 428, 181–187.
- Saitou, H., Yanagi, H., Hara, S., Tsuchiya, S., Tomura, S., 2000. Cerebral blood volume and oxygenation among poststroke hemiplegic patients: effects of 13 rehabilitation tasks measured by near-infrared spectroscopy. *Arch. Phys. Med. Rehabil.* 81, 1348–1356.
- Sakatani, K., Chen, S., Lichty, W., Zuo, H., Wang, Y.P., 1999. Cerebral blood oxygenation changes induced by auditory stimulation in newborn infants measured by near infrared spectroscopy. *Early Hum. Dev.* 55, 229–236.
- Sato, H., Takeuchi, T., Sakai, K.L., 1999. Temporal cortex activation during speech recognition: an optical topography study. *Cognition* 73, B55–B66.
- Schweiger, M., Arridge, S.R., Nissila, I., 2005. Gauss–Newton method for image reconstruction in diffuse optical tomography. *Phys. Med. Biol.* 50 (10), 2365–2386.
- Shah, N., Cerussi, A.E., Jakubowski, D., Hsiang, D., Butler, J., Tromberg, B.J., 2004. Spatial variations in optical and physiological properties of healthy breast tissue. *J. Biomed. Opt.* 9 (3), 534–540.
- Sokol, D.K., Markand, O.N., Daly, E.C., Luerssen, T.G., Malkoff, M.D., 2000. Near infrared spectroscopy (NIRS) distinguishes seizure types. *Seizure* 9, 323–327.
- Srinivasan, S., Pogue, B.W., Jiang, S., Dehghani, H., Kogel, C., Soho, S., Gibson, J.J., Tosteson, T.D., Poplack, S.P., Paulsen, K.D., 2003. Interpreting hemoglobin and water concentration, oxygen saturation, and scattering measured in vivo by near-infrared breast tomography. *Proc. Natl. Acad. Sci.* 100 (21), 12349–12354.
- Steinhoff, B.J., Herrendorf, G., Kurth, C., 1996. Ictal near infrared spectroscopy in temporal lobe epilepsy: a pilot study. *Seizure* 5, 97–101.
- Strangman, G., Culver, J.P., Thompson, J., Boas, D.A., 2002. A quantitative comparison of simultaneous BOLD fMRI and NIRS recordings during functional brain activation. *NeuroImage* 17, 719–731.
- Strangman, G., Franceschini, M.A., Boas, D.A., 2003. Factors affecting the accuracy of near-infrared spectroscopy concentration calculations for focal changes in oxygenation parameters. *NeuroImage* 18, 865–879.
- Taga, G., Asakawa, K., Maki, A., Konishi, Y., Koizumi, H., 2003. Brain imaging in awake infants by near-infrared optical topography. *Proc. Natl. Acad. Sci.* 100, 10722–10727.
- Toronov, V., Franceschini, M., Filiaci, M., Fantini, S., Wolf, M., Michalos, A., Gratton, E., 2000. Near-infrared study of fluctuations in cerebral hemodynamics during rest and motor stimulation: temporal analysis and spatial mapping. *Med. Phys.* 27 (4), 801–815.
- Uludag, K., Kohl, M., Steinbrink, J., Obrig, H., Villringer, A., 2002. Cross talk in the Lambert–Beer calculation for near-infrared wavelengths estimated by Monte Carlo simulations. *J. Biomed. Opt.* 7, 51–59.
- Ursino, M., Colantuoni, A., Bertuglia, S., 1998. Vasomotion and blood flow regulation in hamster skeletal muscle microcirculation: a theoretical and experimental study. *Microvasc. Res.* 56, 233–252.
- Verlaan, M., Heemink, A.W., 1997. Tidal flow forecasting using reduced rank square root filters. *Stoch. Hydrol. Hydraul.* 5, 349–368.
- Vernieri, F., Rosato, N., Pauri, F., Tibuzzi, F., Passarelli, F., Rossini, P.M., 1999. Near infrared spectroscopy and transcranial Doppler in monohemispheric stroke. *Eur. Neurol.* 41, 159–162.
- Watanabe, E., Maki, A., Kawaguchi, F., Yamashita, Y., Koizumi, H., Mayanagi, Y., 2000. Noninvasive cerebral blood volume measurement during seizures using multichannel near infrared spectroscopic topography. *J. Biomed. Opt.* 5, 287–290.
- Worsley, K.J., Friston, K.J., 1995. Analysis of fMRI time-series revisited—again. *NeuroImage* 2 (3), 173–181.
- Xu, H., Springett, R., Dehghani, H., Pogue, B.W., Paulsen, K.D., Dunn, J.F., 2005. Magnetic-resonance-imaging-coupled broadband near-infrared tomography system for small animal brain studies. *Appl. Opt.* 44 (11), 2177–2188.
- Yamamoto, T., Maki, A., Kadoya, T., Tanikawa, Y., Yamada, Y., Okada, E., Koizumi, H., 2002. Arranging optical fibres for the spatial resolution improvement of topographical images. *Phys. Med. Biol.* 47, 3429–3440.
- Zhang, Q., Brukilacchio, T.J., Li, A., Stott, J., Chaves, T., Hillman, E., Wu, T., Chorlton, M., Rafferty, E., Moore, R.H., Kopans, D.B., Boas, D.A., 2005a. Coregistered tomographic X-ray and optical breast imaging: initial results. *J. Biomed. Opt.* 10 (2), 024033.
- Zhang, Y., Brooks, D.H., Franceschini, M.A., Boas, D.A., 2005b. Eigenvector-based spatial filtering for reduction of physiological interference in diffuse optical imaging. *J. of Biomed. Opt.* 10 (1), 011014.
- Zhang, Y., Brooks, D.H., Boas, D.A., 2005c. A hemodynamic response function model in spatio-temporal diffuse optical tomography. *Phys. Med. Biol.* 50 (19), 4625–4644.
- Zwiener, U., Schelenz, C., Bramer, S., Hoyer, D., 2001. Short-term dynamics of relative coordination between respiratory movements, heart rate and arterial pressure fluctuations within the respiratory frequency range. *Physiol. Res.* 50, 59–69.